INORGANIC CHEMISTRY FRONTIERS

RESEARCH ARTICLE

View Article Online
View Journal | View Issue

Open Access Article. Published on 18 March 2025. Downloaded on 3/10/2026 11:04:16 PM.
This article is licensed under a Creative Commons Attribution-NonCommercial 3.0 Unported Licence.

Check for updates

Cite this: *Inorg. Chem. Front.*, 2025, **12**, 3898

Gallium incorporation in blue-emitting $In_{1-x}Ga_xP$ alloy quantum dots facilitated by monomeric gallium precursors†

Taewan Kim,[a] Se-Yup Kim,[a] Sooho Lee,[b] Ji-Sang Park,[c] Hyeonjun Lee*[d] and Doh C. Lee *[a]

Received 28th January 2025,
Accepted 18th March 2025

DOI: 10.1039/d5qi00302d

rsc.li/frontiers-inorganic

Demand for environmentally friendly quantum dots (QDs) in wide color-gamut displays has led to successful development of red- and green-emitting InP QDs with outstanding optical properties. While progress in developing blue-emitting variants remains challenging, $In_{1-x}Ga_xP$ alloy QDs have recently garnered attention as blue emitters. However, Ga incorporation in these $In_{1-x}Ga_xP$ QDs is hindered by the limited reactivity of conventional gallium halide-derived precursors having a dimeric molecular structure. Here, we adopt trimethylgallium which yields monomeric gallium carboxylates as a Ga precursor in the colloidal synthesis of $In_{1-x}Ga_xP$ QDs. This approach promotes efficient Ga incorporation into $In_{1-x}Ga_xP$ QDs with narrow size distributions. The use of zinc chloride and oleylamine for ZnS shell growth on the $In_{1-x}Ga_xP$ cores further adjusts the photoluminescence (PL) wavelength to the blue range and enhances PL quantum yield. The resulting $In_{1-x}Ga_xP$/ZnS core/shell QDs exhibit a peak emission at 470 nm, 67% of photoluminescence quantum yield, and 40 nm of emission linewidth. Successful employment of these QDs into light-emitting diodes demonstrates their potential as a blue electroluminescent emitter for future QD displays.

1 Introduction

As colloidal quantum dot (QD) emitters gain prominence in wide color-gamut display technology, efforts to develop environmentally friendly QDs have rapidly intensified.[1,2] Consequently, red- and green-emitting Cd-free QDs have achieved remarkable progress,[3–5] driving the successful commercialization of photoluminescence (PL)-based QD display technology.[6,7] QD display technology is set to advance beyond its current photoluminescence-based applications toward electroluminescent devices, underscoring the need for environmentally friendly blue-emitting QDs.[8,9]

One prominent outcome of the efforts for developing blue-emitting QDs is the emergence of Zn chalcogenide-based QDs. ZnSe QDs, with a bulk band gap (E_g) of 2.7 eV, typically emit in the near-ultraviolet region, and various strategies have been employed to shift this emission into the blue range. These include controlling nanocrystal growth chemistry to synthesize ZnSe QDs with near-bulk dimensions (~10 nm),[10] and alloying ZnSe with ZnTe (with a bulk E_g of 2.26 eV) to synthesize $ZnSe_{1-x}Te_x$ alloy QDs.[11,12] Despite these advances, Zn chalcogenide QDs continue to face critical challenges; $ZnSe_{1-x}Te_x$ QDs exhibit emissions from localized states caused by inhomogeneous Te doping, and Zn chalcogenide QDs demonstrate relatively low photo-[13] or electro-chemical stability.[14,15]

III–V group QDs with a covalent nature, such as $In_{1-x}Ga_xP$ alloy QDs, are emerging as an alternative composition for blue QD emitters. Single-composition InP (with a bulk E_g of 1.35 eV and an exciton Bohr radius of ~10 nm) is theoretically available for blue emission with a sub-2 nm diameter[16] at which, the nanocrystals are not only thermodynamically unstable due to a very high surface-to-volume ratio but also energetically competitive with metastable magic size clusters.[17] Uniform alloying of GaP into the InP lattice can address these thermodynamic limitations. The incorporation of GaP with a wider E_g (2.24 eV) successfully shifts the E_g of InP QDs into the blue emission region.[18]

However, a key challenge remains in achieving the incorporation of Ga ions within $In_{1-x}Ga_xP$ QDs. Conventional gallium

[a]Department of Chemical and Biomolecular Engineering, KAIST Institute for the Nanocentury, Energy and Environmental Research Center (EERC), KAIST Graduate School of Semiconductor Technology, Korea Advanced Institute of Science and Technology (KAIST), Daejeon 34141, Republic of Korea. E-mail: dclee@kaist.edu
[b]Samsung Display Research Center, Samsung Display, Yongin, Republic of Korea
[c]SKKU Advanced Institute of Nanotechnology (SAINT), Sungkyunkwan University (SKKU), Suwon 16419, Republic of Korea
[d]Department of Energy Science and Center for Artificial Atoms, Sungkyunkwan University, Suwon 16419, Republic of Korea. E-mail: lhj9269@skku.edu
† Electronic supplementary information (ESI) available. See DOI: https://doi.org/10.1039/d5qi00302d

 This journal is © the Partner Organisations 2025

Open Access Article. Published on 18 March 2025. Downloaded on 3/10/2026 11:04:16 PM.
This article is licensed under a Creative Commons Attribution-NonCommercial 3.0 Unported Licence.

halide-mediated precursors, widely used in bottom-up colloidal synthesis,[19] generally exhibit lower chemical reactivity compared to their In counterparts, leading to very low Ga incorporation[20,21] or nonuniform GaP alloying that results in a core/shell-like structure.[22] Wegner *et al.* pointed out the low reactivity of the gallium halide-mediated precursors due to their dimeric structure, which features bridging halides and requires high activation energy for decomposition.[20] However, it remains unclear how the structural characteristics of gallium precursors affect the synthesis of $In_{1-x}Ga_xP$ QDs.

A top-down synthesis of $In_{1-x}Ga_xP$ QDs *via* cation exchange reaction is considered a potential strategy to address the reactivity differences between In and Ga precursors.[18,23–25] In the cation exchange process, Ga^{3+} ions substitute In^{3+} ions in the pre-synthesized host lattice of InP QDs, which is driven by Pearson's hard–soft acid–base theory.[26–28] However, this method poses challenges in achieving spatial control of guest cations within the host lattice, as the incorporation of the guest cation has to be initiated from the surface of QDs.[29,30] In addition, it is hard to directly integrate this post-synthetic process into the current mass production systems for QDs, based on the bottom-up colloidal synthesis. Such limitations speak volumes about the necessity for appropriate Ga precursors, enabling efficient Ga incorporation in the colloidal synthesis of $In_{1-x}Ga_xP$ QDs.

Herein, we addressed the challenge of the low reactivity of gallium halide-based precursors during the bottom-up colloidal synthesis of blue-emitting $In_{1-x}Ga_xP$ QDs by employing monomeric Ga precursors derived from organometallic trimethylgallium (TMGa). Unlike gallium carboxylates produced from gallium iodide, which maintain a dimeric structure with bridging iodides and di-substituted carboxylate groups, gallium carboxylates derived from TMGa adopt a monomeric structure with fully substituted carboxylate groups. These monomeric precursors react with indium carboxylates and phosphorus precursors at 300 °C to produce $In_{1-x}Ga_xP$ alloy QDs with a narrow size distribution and uniform composition. The photoluminescence properties of the $In_{1-x}Ga_xP$ QDs were further enhanced through ZnS shell growth utilizing zinc chloride and oleylamine. The resulting $In_{1-x}Ga_xP$/ZnS core/shell QDs were successfully integrated into electroluminescent devices, demonstrating their potential to be widely applied in electroluminescent QD displays.

2 Experimental methods

2.1 Materials

Zinc stearate ($Zn(St)_2$, 99%), lauric acid (LA, 98%), oleylamine (OAm, 70%), 1-dodecanethiol (DDT, ≥98%), 2-ethylhexanoic acid (2-EHA, 99%), sodium hydroxide (NaOH, ≥98%), gallium (III) iodide (GaI_3, 99.99%), zinc acetate dihydrate ($Zn(Ac)_2{\cdot}2H_2O$, ≥99%), magnesium acetate tetrahydrate ($Mg(Ac)_2{\cdot}4H_2O$, ≥99%), tetramethylammonium hydroxide (TMAH, ≥99%), and molybdenum(VI) oxide (MoO_3, ≥99.9%) were purchased from Sigma-Aldrich. Anhydrous zinc chloride ($ZnCl_2$, 98%) and oleic acid (OA, 90%) were purchased from Alfa Aesar. Tris(trimethylsilyl)phosphine (TMS_3P, 97%) was purchased from LABCARE. Trimethylgallium (TMGa, 99%) was obtained from ICHEMS. Indium acetate ($In(Ac)_3$, 99%), zinc acetate ($Zn(Ac)_2$, ≥99%), 1-octadecene (ODE, 98%), and trioctylphosphine (TOP, ≥97.5%) were supplied by UNIAM. Aluminum (Al, ≥99.9%) and 4,4′-bis(*N*-carbazolyl)-1,1′-biphenyl (CBP, ≥99.5%) were purchased from Lumtec. All other organic solvents were obtained from Samchun Chemicals. All chemicals were used as received without further purification.

2.2 *Ex situ* synthesis of gallium carboxylates using GaI_3 and TMGa

To synthesize gallium carboxylates, 2 mmol of GaI_3 were dissolved in 20 mL of anhydrous methanol under stirring at room temperature. Subsequently, desired equivalents of 2-EHA and NaOH relative to GaI_3 were sequentially added into the solutions. The mixture was allowed to react at room temperature for 1 hour, during which the formation of a white precipitate of gallium carboxylates was observed. The precipitate was collected, washed five times with anhydrous methanol, and dried under vacuum for subsequent analysis.

To synthesize gallium carboxylates using TMGa, TMGa dissolved in TOP was reacted with a desired equivalent of 2-EHA, and the reaction was performed at 200 °C for 1 hour. The obtained gallium carboxylates were filtered out using methanol and further washed with methanol ten times. The precipitate was dried under vacuum for subsequent analysis.

2.3 Synthesis of $In_{1-x}Ga_xP$ alloy QDs

All syntheses were conducted using standard Schlenk line equipment. Indium laurate ($In(LA)_3$) was prepared by reacting 2 mmol of $In(Ac)_3$ with 6 mmol of LA in 6 mL of ODE under vacuum (≤200 mTorr) for 2 hours. Gallium laurate ($Ga(LA)_3$) was prepared by reacting 5 mmol of 1.0 M TMGa dissolved in TOP with 15 mmol of LA in 10 mL of ODE at 200 °C for 30 minutes under a N_2 atmosphere.

To synthesize $In_{1-x}Ga_xP$ cores for blue emission, 2 mmol of $Zn(St)_2$ was dissolved in 16 mL of ODE and degassed at 110 °C for 30 minutes.[31] Subsequently, 2 mmol each of $In(LA)_3$ and $Ga(LA)_3$ were added to the reaction flask and further degassed at 110 °C for 30 minutes. The reaction flask was then heated to 300 °C under a N_2 atmosphere and held for 1 hour to complete the formation of metal carboxylates. After the reaction temperature was lowered to 110 °C, 3 mL of 0.33 M TMS_3P dissolved in TOP was injected and held for 20 minutes. The reaction flask was then reheated to 300 °C, yielding $In_{1-x}Ga_xP$ cores. After the reaction, the flask was rapidly cooled down to room temperature. The solution was purified twice using a precipitation/redispersion method with anhydrous EtOH/toluene. The purified cores were redispersed in toluene and stored in a glove box for shell growth.

2.4 ZnS shell growth on $In_{1-x}Ga_xP$ cores

0.5 M $ZnCl_2$ solution was prepared by dissolving 5 mmol of $ZnCl_2$ in 10 mL of TOP or OAm under stirring at 100 °C in a

Open Access Article. Published on 18 March 2025. Downloaded on 3/10/2026 11:04:16 PM.
This article is licensed under a Creative Commons Attribution-NonCommercial 3.0 Unported Licence.

nitrogen-filled glove box. 0.5 M $Zn(OA)_2$ was prepared by degassing 5 mmol of $Zn(Ac)_2$ and 10 mmol of OA in 6.8 mL of TOA at 160 °C for 2 hours.

To grow ZnS shells on $In_{1-x}Ga_xP$ QD cores, 0.37 mL of $In_{1-x}Ga_xP$ cores (optical density of 1.55 at 380 nm) were dissolved in 10 mL of ODE in a three-necked round-bottom flask and degassed at 110 °C for 30 minutes. For surface-treatment of the cores, 1 mL of 0.5 M $ZnCl_2$ dissolved in TOP was injected into the flask and further degassed for 30 minutes. Backfilling N_2, 1.5 mL of $ZnCl_2$ dissolved in OAm and 0.19 mL of DDT were added. The reaction flask was heated up to 300 °C and held for 2 hours, which yields the ZnS inner shell. Then, for the growth of the ZnS thick shell, 2.4 mL of 0.5 M $Zn(OA)_2$ and 0.29 mL of DDT were dropwise injected into the flask at 300 °C and the reaction was continued for another 20 minutes. After the shell growth was finished, the solution was rapidly cooled down to room temperature and purified twice using a precipitation/redispersion method with acetone/toluene. The purified $In_{1-x}Ga_xP$/ZnS QDs were dispersed in *n*-octane and stored in a glove box for further use.

2.5 Fabrication of QLEDs

Zinc magnesium oxide (ZnMgO) nanoparticles, used as an electron transport layer (ETL), were synthesized with minor modifications based on a literature method.[32] Specifically, 5.1 mmol of $Zn(Ac)_2{\cdot}2H_2O$ and 0.9 mmol of $Mg(Ac)_2{\cdot}4H_2O$ were dissolved in 60 mL of DMSO at 60 °C until completely dissolved. Then, 10 mmol of 0.5 M TMAH dissolved in EtOH was rapidly injected into the DMSO solution and reacted for 1 hour, yielding ZnMgO nanoparticles. The nanoparticles were collected by washing twice with acetone and redispersed in EtOH.

To fabricate QLEDs, 33 nm-thick ZnMgO nanoparticle ETLs were spin-coated onto indium-tin-oxide (ITO) substrates at 4000 rpm for 30 seconds, followed by annealing at 150 °C for 25 minutes. QD emissive layers of 1.5 monolayers were deposited by spin-coating an $In_{1-x}Ga_xP$/ZnS QD solution at 4000 rpm for 30 seconds, followed by annealing at 90 °C for 25 minutes. The spin-coated substrates were then transferred to a thermal evaporator, where 60 nm of CBP, 10 nm of MoO_3, and 100 nm of an Al electrode were deposited under a vacuum of 1×10^{-6} Torr at evaporation rates of 1.5, 0.2, and 2.0 Å s^{-1}, respectively. The fabricated devices were encapsulated with UV-curable resin and glass lids, and then stored in a glove box for further characterization.

2.6 Characterization

Elemental analysis of gallium carboxylates was performed using a Thermo Fisher Scientific FlashSmart elemental analyzer. X-ray photoelectron spectroscopy (XPS) was conducted with Thermo VG Scientific K-alpha. Fourier transform infrared (FTIR) spectroscopy was performed with Thermo Fisher Nicolet iS50. Laser desorption ionization time of flight (LDI-TOF) mass spectrometry was conducted with Bruker autoflex maX. UV-vis absorption spectroscopy was conducted with a Shimadzu UV-2600i spectrophotometer. PL spectroscopy and PL quantum yield (QY) measurements were carried out using a Hamamatsu absolute PL quantum yield spectrometer C11347 at an excitation wavelength of 365 nm. Time-resolved PL measurement was performed using a light conversion femtosecond laser (PHAROS) coupled with a PicoQuant time-correlated single-photon counting system. The laser output was converted to the excitation wavelength of 365 nm using a light conversion collinear optical parametric amplifier (ORPHEUS). Transmission electron microscopy (TEM) was conducted using an FEI Tecnai F20 microscope operating at 200 kV. Inductively coupled plasma optical emission spectrometry (ICP-OES) was performed with an Agilent ICP-OES 5110. For ICP-OES analysis, samples were digested in aqua regia (a mixture of hydrochloric acid and nitric acid in a volume ratio of 3 : 1) and diluted with deionized water. X-ray diffraction (XRD) spectroscopy was conducted with a RIGAKU Ultima IV system under Cu Kα irradiation. Ultraviolet photoelectron spectroscopy (UPS) measurements were performed with a Thermo Scientific Nexsa G2 using a He I photon source (21.2 eV). The electroluminescence characteristics of blue-emitting quantum dot light-emitting diodes (QLEDs) were measured using a Konica Minolta CS-2000 spectroradiometer coupled with a Keithley 2450 SourceMeter.

2.7 Energy change calculation in the reaction of gallium precursors using density functional theory (DFT)

We performed first-principles density functional theory calculations by using the projector augmented wave method (PAW)[33] as implemented in the Vienna *ab initio* simulation package (VASP).[34] We used an exchange–correlation functional parametrized by Perdew, Burke, and Ernzerhof[35] and the DFT-D3 method with Becke–Johnson damping function for a better description of dispersion interaction.[36] The plane waves were expanded up to 400 eV. The atomic structures were optimized until the residual forces became less than 0.01 eV $Å^{-1}$.

3 Results and discussion

3.1 Structures of gallium carboxylates derived from gallium iodide and TMGa

Solid-state gallium halides are predominantly stable as a structure of Ga_2X_6 dimers (X = Cl, Br, or I) rather than GaX_3 monomers in equilibrium (Fig. 1a).[37,38] Our first-principles DFT calculations support that Ga_2I_6 dimers are more preferred than monomeric GaI_3. The energy change (ΔE) in the dimerization of GaI_3 is calculated to be −0.839 eV (Fig. S1a†). Previous studies have suggested that the reaction of these Ga_2X_6 dimers with carboxylic acids results in the partial substitution of only two halogen atoms with carboxylate groups.[20] To quantitatively examine the carboxylate substitution, we *ex situ* synthesized gallium carboxylates derived from gallium iodide by reacting them with 2-EHA in a methanol medium (Fig. 1a, see Experimental methods).[39] To ensure complete carboxylate substitution, an excess amount of sodium 2-ethylhexanoate, exceeding three equivalents, was reacted with gallium iodide.

Open Access Article. Published on 18 March 2025. Downloaded on 3/10/2026 11:04:16 PM.
This article is licensed under a Creative Commons Attribution-NonCommercial 3.0 Unported Licence.

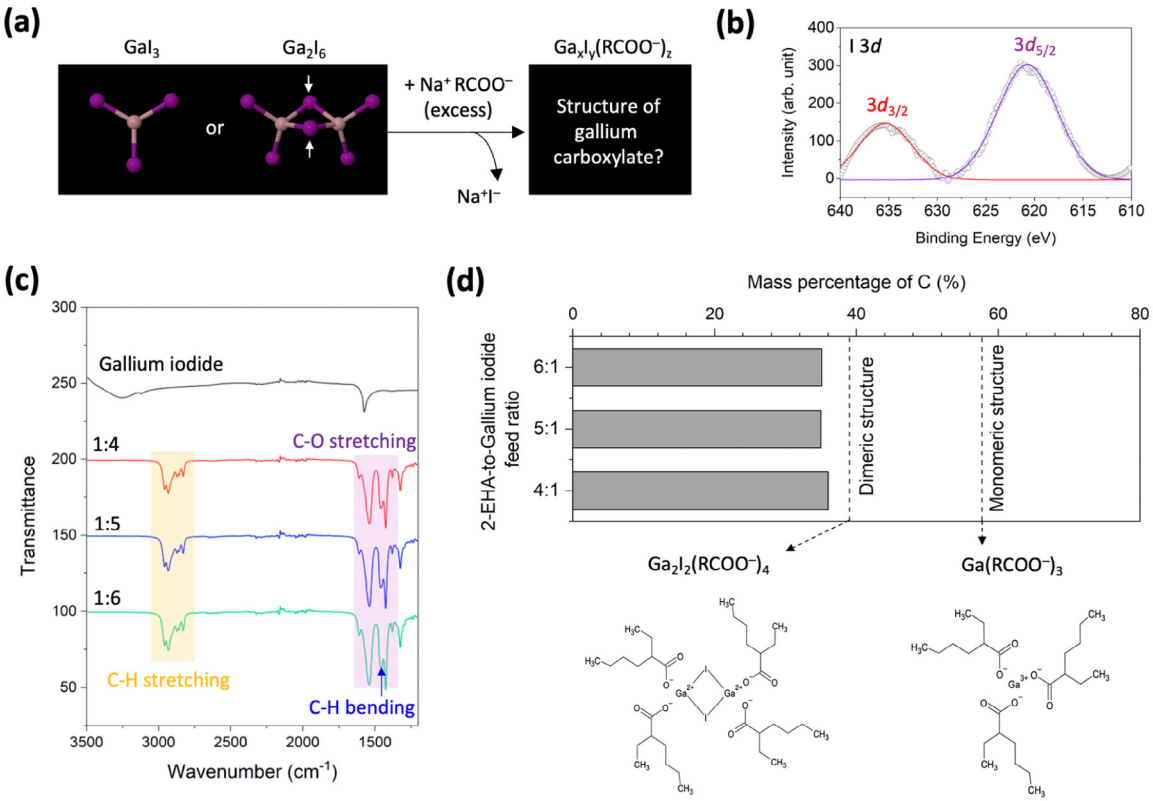

Fig. 1 Structure of gallium carboxylates derived from a gallium iodide. (a) Schematic illustration of the carboxylate substitution reaction of gallium iodide which exists as monomeric GaI_3 or dimeric Ga_2I_6. The bridging halides in Ga_2I_6 are indicated with white arrows. (b) XPS spectrum of the I 3d core-level region of gallium 2-ethylhexanoate derived from gallium iodide (circles). The I $3d_{3/2}$ (red) and I $3d_{5/2}$ (purple) orbitals were deconvoluted. (c) FTIR spectra of gallium 2-ethylhexanoate derived from gallium iodide with varying feed ratios of gallium iodide to 2-ethylhexanoic acid (1 : 4, 1 : 5, and 1 : 6). (d) Mass percentage of carbon in gallium 2-ethylhexanoate (upper panel). The black dashed lines indicate the calculated mass percentages of carbon for the proposed structures of dimeric and monomeric gallium 2-ethylhexanoates (lower panel).

We first conducted XPS measurements for the I 3d core-level to assess the substitution of iodide to the carboxylate group. The XPS spectra demonstrate the I 3d orbitals, revealing that the iodine atoms still remain in gallium carboxylates (Fig. 1b).[40] The FTIR spectra for gallium carboxylates exhibit distinctive vibrational peaks corresponding to C–H stretching (2990–2850 cm^{-1}), C–O stretching (1600–1500 cm^{-1} and 1430–1400 cm^{-1}), and C–H bending (1462 cm^{-1}), indicative of carboxylate groups (Fig. 1c).[41] These results suggest that not all the iodide groups in gallium iodide were fully replaced by carboxylate groups, but were only partially substituted.

The elemental analysis result demonstrates that the weight percent of carbon in gallium carboxylates derived from gallium iodide was approximately 36%, regardless of the excess amount of reacting 2-EHA (Fig. 1d and Table S1†). This value is significantly lower than the theoretical carbon content of monomeric gallium tri-2-ethylhexanoate (57.7%, right lower panel in Fig. 1d). In the dimeric structure of gallium halides, the halogen atoms bridging the two gallium centers, known as bridging halides, are strongly bound to the Ga atoms.[37,38] The large activation energy required for the dissociation of bridging halides contributes to the formation of dimeric and partially substituted precursors with a structure of $Ga_2I_2(RCOO^-)_4$ (left lower panel in Fig. 1d). This structure theoretically has a carbon mass percentage of 39%, which is close to the 36% carbon content in the analyzed gallium 2-ethylhexanoates derived from gallium iodide. We attribute the discrepancy in the carbon mass percentage to the contribution from a minor portion of mono-substituted gallium carboxylates.

To investigate the carboxylate substitution of a monomeric Ga compound and thereby to circumvent the challenges of bridging halide dissociation in gallium halides, we selected TMGa as a suitable candidate. While various organometallic compounds (*e.g.*, diethylzinc or dimethylcadmium) have been employed in the colloidal synthesis of QDs,[42–44] the application of TMGa in this field remains largely unexplored.

We also performed first-principles DFT calculations to evaluate the energy change in dimerization (Fig. S1b†) and gallium tri-2-ethylhexanoate formation reaction (Fig. S1c†) from monomeric TMGa. The energy change in the dimerization of TMGa is calculated to be 0.934 eV, which is thermodynamically unfavorable (Fig. S1b†). In contrast, the formation

Open Access Article. Published on 18 March 2025. Downloaded on 3/10/2026 11:04:16 PM.
This article is licensed under a Creative Commons Attribution-NonCommercial 3.0 Unported Licence.

of gallium tri-2-ethylhexanonoates is highly favorable, with an energy change of −3.769 eV. These results suggest that monomeric TMGa would enable efficient carboxylate substitution, leading to the formation of gallium tri-carboxylates.

The FTIR spectra of TMGa and its derivative, gallium 2-ethylhexanoate, both exhibit identical vibrational peaks corresponding to C–H stretching and C–H bending of the methyl and 2-EHA groups (Fig. S2†). However, following the carboxylate substitution reaction, gallium 2-ethylhexanoate exhibits a distinctive C–O stretching peak, indicating that the carboxylate groups have replaced the methyl groups in TMGa. The LDI-TOF analysis of gallium 2-ethylhexanoates derived from TMGa reveals a sharp peak at 497.52 *m*/*z* (Fig. S3†) which greatly approximates the molar mass of ~500 Da of gallium tri-2-ehtylhexanoate. These results suggest that gallium 2-ethylhexanoate derived from TMGa has a monomeric structure, with the methyl groups fully substituted by carboxylates (Fig. 1d, lower right).

3.2 Synthesis of $In_{1-x}Ga_xP$ alloy QDs using monomeric and dimeric gallium carboxylates

We synthesized $In_{1-x}Ga_xP$ QDs using monomeric and dimeric gallium carboxylates derived from TMGa and gallium iodides, respectively (Fig. 2a). The QD synthetic scheme was modified from the well-established bottom-up colloidal synthesis of InP QDs, which utilizes metal carboxylates and TMS_3P as precursors (Fig. 2a, see the Experimental methods).[45] To investigate the optical properties of the QDs as a function of Ga content, we varied the Ga-to-In feed ratios to 1, 2, and 3 while maintaining the total amount of Ga and In precursors constant.

The absorption spectra demonstrate that the 1S transition peak wavelength of the QDs blue-shifted with increasing Ga-to-In feed ratios, regardless of the type of gallium carboxylate used (Fig. 2b). However, the 1S transition peak wavelength of QDs using monomeric $Ga(LA)_3$ was 30–40 nm shorter than that of QDs using dimeric $Ga_2I_2LA_4$. This suggests that for the same Ga-to-In feed ratio, Ga incorporation into QDs was more efficient when using monomeric $Ga(LA)_3$ compared to that with dimeric $Ga_2I_2LA_4$. The half-width at half-maximum (HWHM) of the absorption peaks of monomeric precursor-based QDs was significantly narrower (with a smaller valley-to-peak ratio in the absorption spectra) compared to that of dimeric precursor-based QDs with similar 1S transition energies (Fig. S4†). This result indicates that the monomeric gallium precursor produces QDs with a narrow size distribution (inset image in Fig. 2b).

We attribute the superior optical properties of TMGa-mediated $In_{1-x}Ga_xP$ QDs to the monomeric structure of gallium carboxylates. Monomeric $Ga(LA)_3$ could effectively decompose during the early stages of the nucleation and subsequent growth of QDs, enabling uniform incorporation of Ga. In contrast, the decomposition of bridging halides in the dimeric gallium carboxylate requires high temperatures close to 300 °C,[46] at which point a vast majority of indium and phosphorus precursors are already consumed by QD formation. The robust bonding configurations of bridging halides exacerbate the reactivity difference between indium and gallium precursors, leading to nonuniform Ga incorporation. To additionally testify whether the monomeric structure in gallium precursors plays a decisive role in efficient Ga incorporation into QDs, we also synthesized $In_{1-x}Ga_xP$ QDs using monomeric gallium acetylacetonate ($Ga(acac)_3$) as a replacement of TMGa. The resulting optical properties were similar to those of QDs synthesized with TMGa (Fig. S5†).

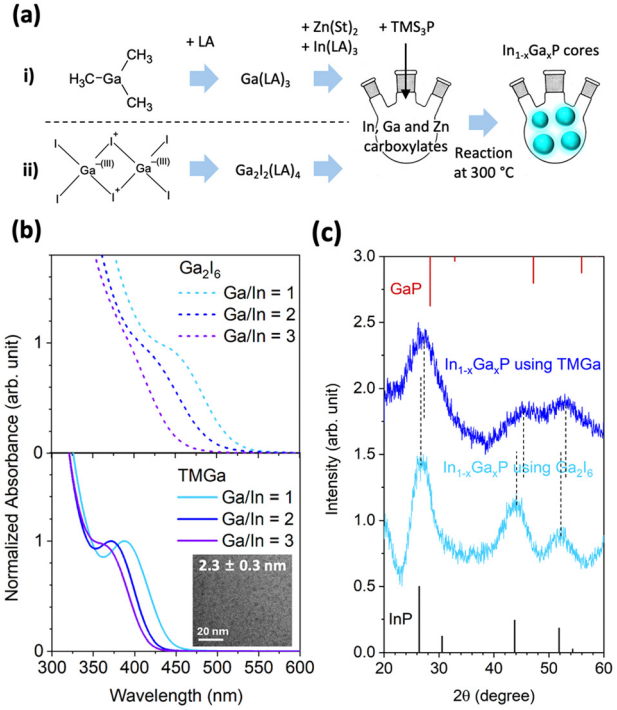

Fig. 2 Synthesis and characterization of $In_{1-x}Ga_xP$ alloy QDs using gallium carboxylates. (a) Schematic illustration of the synthetic procedure of $In_{1-x}Ga_xP$ alloy QDs using (i) TMGa and (ii) Ga_2I_6. (b) UV-vis absorption spectra of $In_{1-x}Ga_xP$ QDs using Ga_2I_6 (dashed lines, upper panel) and TMGa (solid lines, lower panel) according to the Ga-to-In feed ratio. The inset shows the transmission electron microscopy image of $In_{1-x}Ga_xP$ QDs using TMGa whose Ga-to-In reed ratio is 1. (c) X-ray diffraction spectra of $In_{1-x}Ga_xP$ QDs. The vertical solid lines represent the standard JCPDS peaks for InP (black, JCPDS #70-2902) and GaP (red, JCPDS #72-4949). The vertical dashed lines indicate the peak positions of the QDs for visual guidance.

In order to investigate how the gallium precursors affect the crystal properties of $In_{1-x}Ga_xP$ QDs, we performed XRD analysis on the samples (Fig. 2c). Both samples exhibited distinctive diffraction peaks corresponding to the (111), (220), and (311) planes (Fig. 2c, dashed lines), which were positioned between the standard peak positions of zinc blende InP (black vertical lines in Fig. 2c) and GaP (red vertical lines in Fig. 2c). While the diffraction peaks of gallium iodide-mediated QDs were closer to the standard peak positions of InP, the peaks of TMGa-derived QDs shifted toward higher 2θ, closer to the GaP standard peaks. This shift suggests higher Ga content incorporated into $In_{1-x}Ga_xP$ QDs derived from TMGa, resulting in a reduction in *d*-spacing.

Open Access Article. Published on 18 March 2025. Downloaded on 3/10/2026 11:04:16 PM.
This article is licensed under a Creative Commons Attribution-NonCommercial 3.0 Unported Licence.

3.3 Composition analysis of $In_{1-x}Ga_xP$ QDs according to the extent of carboxylate substitution from TMGa

Previous analyses demonstrate that the monomeric structure of gallium carboxylates facilitates Ga incorporation in $In_{1-x}Ga_xP$ QDs. However, a question remains as to how the under-substitution of carboxylate (*e.g.*, di-substitution) from TMGa affects the Ga incorporation into $In_{1-x}Ga_xP$ QDs. To address this question, we synthesized $In_{1-x}Ga_xP$ QDs using di-substituted gallium laurate [*i.e.*, intentionally reacting 2 equivalents of LA with TMGa to produce $Ga(CH_3)(LA)_2$]. Interestingly, the absorption spectra reveal that the wavelength at the 1S transition peaks was seldom changed regardless of the Ga-to-In feed ratio, with only the HWHM of the absorption peaks varying (Fig. S6a†). This result implies that the amount of di-substituted gallium laurate has little influence on the extent of the Ga incorporation into $In_{1-x}Ga_xP$ QDs.

To quantitatively characterize the composition in $In_{1-x}Ga_xP$ QDs, we performed ICP-OES analysis of the QD samples synthesized using $Ga(LA)_3$ and $Ga(CH_3)(LA)_2$ (Table S2† and Fig. 3). When $Ga(LA)_3$ was used, the incorporated Ga-to-In ratio in $In_{1-x}Ga_xP$ linearly increased to $In_{0.6}Ga_{0.4}P$, $In_{0.4}Ga_{0.6}P$, and $In_{0.3}Ga_{0.7}P$ as the feed Ga-to-In ratio increased by 1, 2, and 3, respectively (red squares in Fig. 3). This tendency corresponds to the widening of the optical E_g observed as the Ga-to-In feed ratio increased (Fig. 2b). The reaction yield of Ga (*i.e.*, the incorporated Ga-to-In ratio divided by the fed Ga-to-In ratio) for $Ga(LA)_3$ reached ~71%. This value is significantly higher compared to the ~40% reaction yield typically achieved with gallium halide-based precursors.[47]

When $Ga(CH_3)(LA)_2$ was used with a feed Ga-to-In ratio of 1, $In_{0.5}Ga_{0.5}P$ QDs were produced with a reaction yield of Ga approaching 100% (leftmost triangle in Fig. 3). However, as the Ga-to-In feed ratio increased to 2 and 3, the detected Ga-to-In ratios exceeded the fed Ga-to-In ratio. Considering that TMS_3P is the limiting reagent, this result indicates that TMS_3P selectively reacted with $Ga(CH_3)(LA)_2$ rather than $In(LA)_3$, producing GaP QDs apart from $In_{0.5}Ga_{0.5}P$ QDs. This result is in line with the consistent 1S transition peaks regardless of the amount of $Ga(CH_3)(LA)_2$ (Fig. S6a†). Notably, we could synthesize GaP QDs using only $Ga(CH_3)(LA)_2$ and TMS_3P (Fig. S6a†), even though GaP QDs were typically known to require high formation energies.[48]

To sum up, the under-substitution of carboxylates in monomeric gallium precursors exhibits higher reactivity compared to their fully substituted counterparts. While Ga incorporation into $In_{1-x}Ga_xP$ QDs was more efficient at a low Ga-to-In feed ratio (Ga-to-In ratio of 1) using under-substituted precursors, a separate formation of GaP QDs simultaneously occurred at higher Ga-to-In feed ratios (Ga-to-In ratios of 2 and 3).

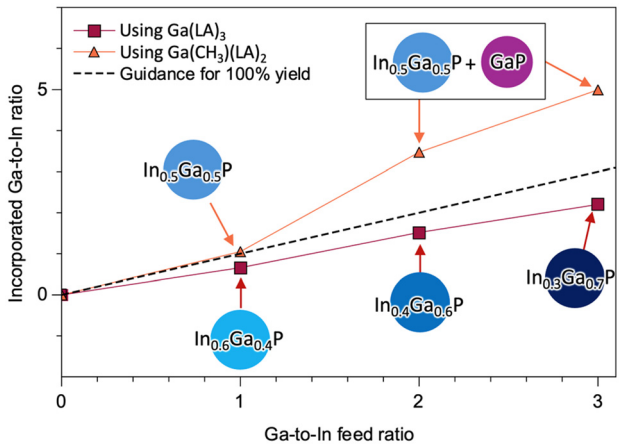

Fig. 3 Incorporated Ga-to-In ratio in $In_{1-x}Ga_xP$ QDs characterized using ICP-OES. The $In_{1-x}Ga_xP$ QDs were synthesized with varying Ga-to-In feed ratios of 1, 2, and 3, using $Ga(LA)_3$ (red squares) and $Ga(CH_3)(LA)_2$ (orange triangles). The dashed line serves as a guide representing unity reaction yield.

3.4 Optical enhancement of $In_{1-x}Ga_xP$/ZnS core/shell QDs using $ZnCl_2$ and their electroluminescence applications

The as-synthesized $In_{1-x}Ga_xP$ QDs exhibit negligible photoluminescence (PL QY of ~1%) due to the nonradiative surface defects.[49,50] Undercoordinated and oxidized surface metal and phosphorus atoms have been generally identified as the primary culprits for nonradiative recombination centers in metal phosphide QDs.[51,52] To address the surface issue of $In_{1-x}Ga_xP$ core QDs, we employed a surface treatment method using zinc halides. The zinc halides act as Z-type ligands, effectively passivating the undercoordinated surface atoms prior to the shell growth (Fig. 4a).[53,54]

Interestingly, we found that the use of $ZnCl_2$ not only passivates the surface but also helps adjust the PL peak wavelength of the $In_{1-x}Ga_xP$/ZnS QDs. Achieving a PL peak within the range of 460 to 475 nm for blue emitters is critical to meet the spectral requirements of the National Television System Committee (NTSC) while avoiding severe damage to the human eye from short-wavelength emissions.[55–57] The use of $Zn(OA)_2$, as a conventional Zn precursor, during ZnS shell growth resulted in QDs with an emission peak exceeding 480 nm (Fig. S7a†), requiring a blue shift of PL by at least 5 nm. This longer PL peak wavelength could be attributed to the binding behavior of the oleate ligand in $Zn(OA)_2$, which acts as a quasi-bidentate ligand due to its chelating geometry.[58] The chelating nature promotes the formation of strong hybrid molecular orbitals with the shell material, leading to enhanced exciton delocalization into the shell.[59,60]

To address the chelation issue, we utilized a $ZnCl_2$–OAm precursor ($ZnCl_2$ dissolved in OAm) as a Zn precursor for shell growth, replacing $Zn(OA)_2$ with a monodentate ligand.[61,62] The monodentate OAm ligand minimized the exciton delocalization by chelation, resulting in a hypsochromic shift of approximately 10 nm, which could then align with the NTSC requirements (solid line in Fig. S7b†). However, after the purification process for the integration into QLEDs, the PL QY of the $In_{1-x}Ga_xP$/ZnS QDs was reduced to nearly half of its initial value (dashed line in Fig. S7b†) due to the detachment of weakly bound OAm ligands on the ZnS shell during the purification process.[63] To prevent ligand detachment after purifi-

Open Access Article. Published on 18 March 2025. Downloaded on 3/10/2026 11:04:16 PM.
This article is licensed under a Creative Commons Attribution-NonCommercial 3.0 Unported Licence.

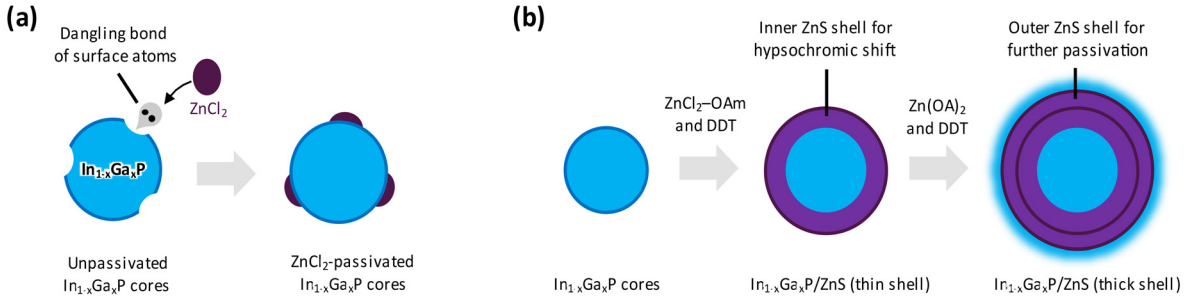

Fig. 4 Schematic illustration of ZnS shell growth on $In_{1-x}Ga_xP$ cores. (a) Surface defect passivation of $In_{1-x}Ga_xP$ cores using $ZnCl_2$. (b) Double-step growth of the ZnS shell using $ZnCl_2$–OAm and $Zn(OA)_2$.

cation, an additional ZnS shell was grown using $Zn(OA)_2$ (Fig. 4b) to ensure effective surface passivation. This modification produced $In_{1-x}Ga_xP$/ZnS core/shell QDs with an average diameter of 6.34 nm, consisting of 2.3 nm $In_{1-x}Ga_xP$ cores and a 2.0 nm ZnS shell (Fig. 5a). The resulting QDs exhibited remarkable optical properties, with an emission peak at 470 nm, a narrow linewidth of 40 nm, and a PL QY of 67% after purification (Fig. 5b). The XRD spectra of the $In_{1-x}Ga_xP$/ZnS QDs were compared with those of the $In_{1-x}Ga_xP$ cores (Fig. 5c). The (111), (220), and (311) diffraction peaks of the zinc blende $In_{1-x}Ga_xP$ cores shifted to higher 2θ values after the growth of ZnS shells. This shift indicates the uniform growth of ZnS thick shell on the $In_{1-x}Ga_xP$ cores, which is responsible for the robust PL properties and narrow linewidths of the $In_{1-x}Ga_xP$/ZnS QDs.

The resulting QDs exhibited one of the narrowest linewidths reported to date among blue-emitting $In_{1-x}Ga_xP$ QDs (Table S4†), highlighting their potential for blue-color reproduction in display technologies. However, the underlying reason for the limited PL QY (67%) of $In_{1-x}Ga_xP$/ZnS QDs, even after uniform ZnS shell growth, remains unclear. We attribute the limited PL QY primarily to the increased contribution

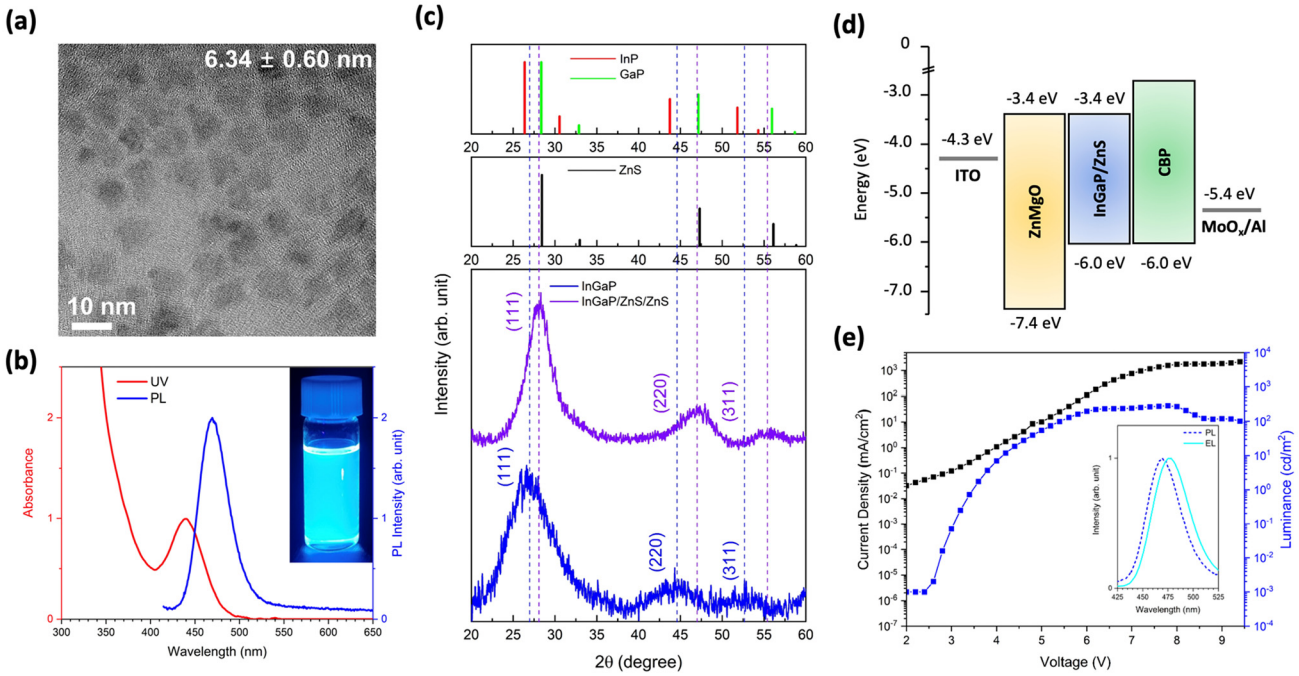

Fig. 5 Characterization of the $In_{1-x}Ga_xP$/ZnS core/shell QDs and their electroluminescence properties. (a) TEM image of $In_{1-x}Ga_xP$/ZnS QDs. (b) UV-vis absorption and PL emission spectra of $In_{1-x}Ga_xP$/ZnS QDs. The PL peak is located at 470 nm, with a FWHM of 40 nm and a PL QY of 67%. The inset photograph demonstrates the $In_{1-x}Ga_xP$/ZnS QDs irradiated with a UV light of 380 nm. (c) XRD spectra of $In_{1-x}Ga_xP$ cores and $In_{1-x}Ga_xP$/ZnS core/shell QDs (lower panel). Standard diffraction peaks for InP (JCPDS #70-2902), GaP (JCPDS #72-4949), and ZnS (JCPDS #86-8464) are provided in the upper panels. Dashed lines indicate the peaks corresponding to the (111), (220), and (311) planes of $In_{1-x}Ga_xP$ cores and $In_{1-x}Ga_xP$/ZnS QDs, respectively. (d) Energy level diagram with respect to a vacuum level for the $In_{1-x}Ga_xP$/ZnS QD-employed QLEDs. The energy levels of $In_{1-x}Ga_xP$/ZnS QDs were characterized using UPS analysis (Fig. S8†). (e) Current (J)–voltage (V)–luminance (L) characteristics of $In_{1-x}Ga_xP$/ZnS QD-employed QLEDs. The inset shows the PL and EL spectra of the QLEDs where the EL spectrum is measured at 6 V.

Open Access Article. Published on 18 March 2025. Downloaded on 3/10/2026 11:04:16 PM.
This article is licensed under a Creative Commons Attribution-NonCommercial 3.0 Unported Licence.

of indirect E_g transition arising from high Ga content in $In_{1-x}Ga_xP$/ZnS QDs.[25] We synthesized $In_{1-x}Ga_xP$/ZnS QDs with varying Ga-to-In feed ratios of 1, 2, and 3 during core synthesis and analyzed their PL characteristics (Fig. S8†). As the Ga-to-In feed ratio increases, the PL spectra blue-shifts (Fig. S8a†), indicating a widened E_g due to a higher amount of Ga incorporated. Concurrently, the PL QY becomes lower (Fig. S8b†). To further elucidate the relationship between Ga content and PL characteristics, we measured time-resolved PL of the samples (Fig. S8c–S8e†). Biexponential fitting of the PL decay curves revealed two distinct decay components (Table S3†): a trap-associated recombination component (1.5–1.6 ns) and a radiative recombination component (45.9–58.7 ns). While the former was relatively consistent regardless of the Ga-to-In ratio, the latter became longer as the ratio increased. The prolonged radiative recombination lifetime, accompanied by a decrease of PL QY, is a distinctive feature of enhanced indirect band gap transition in $In_{1-x}Ga_xP$/ZnS QDs.[25] These results emphasize that precise control of Ga incorporation into $In_{1-x}Ga_xP$ QDs is essential for optimizing both PL QY and emission wavelength to attain efficient blue emission.

Finally, we incorporated the $In_{1-x}Ga_xP$/ZnS QDs into QLEDs with an inverted structure. The device architecture consisted of an ITO cathode, a ZnMgO electron transport layer (ETL), an $In_{1-x}Ga_xP$/ZnS QD emissive layer, a CBP hole transport layer (HTL), and a MoO_3/Al anode (Fig. 5d and Fig. S9†).[18,64,65] Current (J)–voltage (V)–luminance (L) characteristics show that the QLEDs exhibit a low turn-on voltage of 2.6 V which is close to the optical E_g of the QDs (Fig. 5e). The EL peak of the QLEDs exhibits a moderate extent of red shift from 470 nm to 477 nm due to the quantum-confined Stark effect at a high operation voltage of 6 V (Fig. 5c).[66] These electrical advantages are attributed to the well-matched energy levels of $In_{1-x}Ga_xP$/ZnS QDs to those of charge transport layers, leading to the minimal accumulation of drift charges with low carrier injection barriers.[67] Based on the EL properties of our devices (Fig. S10 and Table S5†), we could highlight the potential of $In_{1-x}Ga_xP$/ZnS QDs as promising electroluminescent emitters for future blue QLEDs.

4 Conclusions

In summary, we revealed the structural effect of Ga precursors on the Ga incorporation into the $In_{1-x}Ga_xP$ QDs. Due to the strong bonding of bridge halides in Ga_2I_6, $Ga_2I_2(RCOO^-)_4$ with a dimeric structure is produced after the carboxylate substitution of Ga_2I_6. These dimeric Ga precursors exhibit low reactivity during the synthesis of $In_{1-x}Ga_xP$ QDs, limiting the Ga incorporation. In contrast, monomeric TMGa produced monomeric gallium carboxylates with tri-substituted carboxylates of $Ga(RCOO^-)_3$, facilitating Ga incorporation during the synthesis of $In_{1-x}Ga_xP$ QDs. Meanwhile, partially substituted gallium carboxylates from TMGa (*i.e.*, $Ga(CH_3)(RCOO^-)_2$) led to the formation of separate GaP QDs due to their higher reactivity compared to that of their indium counterparts.

The use of $ZnCl_2$ and OAm in the early stage of ZnS shell growth improved the optical properties of $In_{1-x}Ga_xP$/ZnS core/shell QDs. The $ZnCl_2$–OAm precursors adjusted the emission wavelength to the blue range due to their monodentate coordination characteristics. Additional ZnS outer shell growth further passivated the $In_{1-x}Ga_xP$/ZnS QDs, resulting in efficient and robust PL characteristics, including an emission peak at 470 nm, a linewidth of 40 nm, and a PLQY of 67%. Consequently, the resulting $In_{1-x}Ga_xP$/ZnS QDs were successfully incorporated into the QLEDs. The $In_{1-x}Ga_xP$/ZnS QD-based QLEDs show efficient charge injection characteristics due to the well-balanced energy levels of the QDs with the charge transport layers.

These results highlight the promising operational performance of these devices and reinforce the potential of $In_{1-x}Ga_xP$ QDs as environmentally friendly materials for optoelectronic applications. While further advancements in QD synthesis and device engineering are necessary for commercialization, we believe that this work establishes a solid foundation for the deployment of $In_{1-x}Ga_xP$-based QDs in next-generation display technologies.

Author contributions

T. Kim: investigation, conceptualization, methodology, data curation, writing – original draft, and writing – review and editing. S.-Y. Kim: methodology, data curation, and writing – review and editing. S. Lee: conceptualization, funding acquisition, and writing – review and editing. J.-S. Park: methodology, software, and writing – review and editing. H. Lee: supervision, investigation, conceptualization, methodology, data curation, writing – original draft, and writing – review and editing. D. C. Lee: supervision, conceptualization, project administration, funding acquisition, writing – original draft, and writing – review and editing.

Data availability

The data supporting this article have been included as part of the ESI.†

Conflicts of interest

There are no conflicts to declare.

Acknowledgements

This work was supported by the National Research Foundation of Korea (NRF) grants funded by the Korean government (MSIT) (RS-2021-NR057412 and RS-2022-NR070840). Additional support was provided by the Korea Planning & Evaluation Institute of Industrial Technology (KEIT) funded by the Korean government (MOTIE) (20019417 and RS-2024-

Open Access Article. Published on 18 March 2025. Downloaded on 3/10/2026 11:04:16 PM.
This article is licensed under a Creative Commons Attribution-NonCommercial 3.0 Unported Licence.

00440884) and the Korea Institute for Advancement of Technology (KIAT) grant funded by the Korea Government (MOTIE) (RS-2023-KI002692, HRD Program for Industrial Innovation). We also acknowledge support from Samsung Display Co., Ltd.

References

1 Y. U. Kim, D. Y. Kim, J. W. Park and B. G. Jeong, Heavy-Metal-Free Heterostructured Nanocrystals for Light-Emitting Applications, *Korean J. Chem. Eng.*, 2024, **41**, 3303–3315.

2 Y. Sung, J. Chang, S. Choi and S. Jeong, Synthesis Strategies and Applications of Non-toxic Quantum Dots, *Korean J. Chem. Eng.*, 2024, **41**, 3317–3343.

3 Y.-H. Won, O. Cho, T. Kim, D.-Y. Chung, T. Kim, H. Chung, H. Jang, J. Lee, D. Kim and E. Jang, Highly efficient and stable InP/ZnSe/ZnS quantum dot light-emitting diodes, *Nature*, 2019, **575**, 634–638.

4 J. H. Jo, D. Y. Jo, S. W. Choi, S. H. Lee, H. M. Kim, S. Y. Yoon, Y. Kim, J. N. Han and H. Yang, Highly bright, narrow emissivity of InP quantum dots synthesized by aminophosphine: effects of double shelling scheme and Ga treatment, *Adv. Opt. Mater.*, 2021, **9**, 2100427.

5 H. J. Lee, S. Im, D. Jung, K. Kim, J. A. Chae, J. Lim, J. W. Park, D. Shin, K. Char, B. G. Jeong, J.-S. Park, E. Hwang, D. C. Lee, Y.-S. Park, H.-J. Song, J. H. Chang and W. K. Bae, Coherent heteroepitaxial growth of I-III-VI2 Ag (In,Ga)S2 colloidal nanocrystals with near-unity quantum yield for use in luminescent solar concentrators, *Nat. Commun.*, 2023, **14**, 3779.

6 J. Yang, M. Lee, S. Y. Park, M. Park, J. Kim, N. Sitapure, D. Hahm, S. Rhee, D. Lee, H. Jo, Y. H. Jo, J. Lim, J. Kim, T. J. Shin, D. C. Lee, K. Kwak, J. S. Kwon, B. Kim, W. K. Bae and M. S. Kang, Nondestructive Photopatterning of Heavy-Metal-Free Quantum Dots, *Adv. Mater.*, 2022, **34**, 2205504.

7 B. G. Jeong, J. H. Chang, D. Hahm, S. Rhee, M. Park, S. Lee, Y. Kim, D. Shin, J. W. Park, C. Lee, D. C. Lee, K. Park, E. Hwang and W. K. Bae, Interface polarization in heterovalent core–shell nanocrystals, *Nat. Mater.*, 2022, **21**, 246–252.

8 S. Cho, Y. Kim, S. Lee and J. Y. Woo, Recent Progress in Blue-Emitting Semiconductor Nanocrystal Quantum Dots for Display Applications, *Korean J. Chem. Eng.*, 2024, **41**, 3359–3370.

9 Y. Jeon, H. Ryu and H. Lee, Recent Progress on Blue Quantum Dot Light-Emitting Diodes from Materials to Device Engineering, *Korean J. Chem. Eng.*, 2024, **41**, 3483–3500.

10 M. Gao, H. Yang, H. Shen, Z. Zeng, F. Fan, B. Tang, J. Min, Y. Zhang, Q. Hua, L. S. Li, B. Ji and Z. Du, Bulk-like ZnSe Quantum Dots Enabling Efficient Ultranarrow Blue Light-Emitting Diodes, *Nano Lett.*, 2021, **21**, 7252–7260.

11 B. J. Lee, T. Y. Kim, I. Kim, J. Y. Ryu, S. Jung, J.-U. Park, D. H. Yoon, Y. Choi, S. Y. Lee and T. Kim, Bright and Stable ZnSeTe Core/Shell Quantum Dots Enabled by Surface Passivation with Organozinc Halide Ligands, *Chem. Mater.*, 2023, **36**, 471–481.

12 C. Cheng, B. Yu, F. Huang, L. Gao, K. Cao, P. Zang, K. Zheng and J. Tian, Near–Unity Quantum Yield ZnSeTe Quantum Dots Enabled by Controlling Shell Growth for Efficient Deep–Blue Light–Emitting Diodes, *Adv. Funct. Mater.*, 2024, 2313811.

13 S. Kim, J.-A. Kim, T. Kim, H. Chung, S. Park, S.-M. Choi, H.-M. Kim, D.-Y. Chung and E. Jang, Efficient blue-light-emitting Cd-free colloidal quantum well and its application in electroluminescent devices, *Chem. Mater.*, 2020, **32**, 5200–5207.

14 Y. Bi, S. Cao, P. Yu, Z. Du, Y. Wang, J. Zheng, B. Zou and J. Zhao, Reducing Emission Linewidth of Pure–Blue ZnSeTe Quantum Dots through Shell Engineering toward High Color Purity Light–Emitting Diodes, *Small*, 2023, **19**, 2303247.

15 E.-P. Jang, C.-Y. Han, S.-W. Lim, J.-H. Jo, D.-Y. Jo, S.-H. Lee, S.-Y. Yoon and H. Yang, Synthesis of alloyed ZnSeTe quantum dots as bright, color-pure blue emitters, *ACS Appl. Mater. Interfaces*, 2019, **11**, 46062–46069.

16 E. Cho, H. Jang, J. Lee and E. Jang, Modeling on the size dependent properties of InP quantum dots: a hybrid functional study, *Nanotechnology*, 2013, **24**, 215201.

17 H. H. Ripberger, S. F. Sandeno, F. W. Eagle, H. A. Nguyen and B. M. Cossairt, Structure and Reactivity of II–VI and III–V Magic-Sized Clusters: Understanding and Expanding the Scope of Accessible Form and Function, *Acc. Mater. Res.*, 2024, **5**, 726–738.

18 K.-H. Kim, J.-H. Jo, D.-Y. Jo, C.-Y. Han, S.-Y. Yoon, Y. Kim, Y.-H. Kim, Y. H. Ko, S. W. Kim, C. Lee and H. Yang, Cation-Exchange-Derived InGaP Alloy Quantum Dots toward Blue Emissivity, *Chem. Mater.*, 2020, **32**, 3537–3544.

19 H. Shin, D. Hong, H. Cho, H. Jang, G. Y. Kim, K. M. Song, M.-J. Choi, D. Kim and Y. S. Jung, Indirect-to-direct bandgap transition in GaP semiconductors through quantum shell formation on ZnS nanocrystals, *Nat. Commun.*, 2024, **15**, 8125.

20 K. D. Wegner, S. Pouget, W. L. Ling, M. Carrière and P. Reiss, Gallium–a versatile element for tuning the photoluminescence properties of InP quantum dots, *Chem. Commun.*, 2019, **55**, 1663–1666.

21 Y. Kim, K. Yang and S. Lee, Highly luminescent blue-emitting In 1− x Ga x P@ ZnS quantum dots and their applications in QLEDs with inverted structure, *J. Mater. Chem. C*, 2020, **8**, 7679–7687.

22 J. P. Park, J.-J. Lee and S.-W. Kim, Highly luminescent InP/GaP/ZnS QDs emitting in the entire color range via a heating up process, *Sci. Rep.*, 2016, **6**, 30094.

23 V. Srivastava, V. Kamysbayev, L. Hong, E. Dunietz, R. F. Klie and D. V. Talapin, Colloidal chemistry in molten salts: Synthesis of luminescent In1−x Ga x P and In1−x Ga x As quantum dots, *J. Am. Chem. Soc.*, 2018, **140**, 12144–12151.

24 M. H. Hudson, A. Gupta, V. Srivastava, E. M. Janke and D. V. Talapin, Synthesis of In1−x Ga x P Quantum Dots in

Open Access Article. Published on 18 March 2025. Downloaded on 3/10/2026 11:04:16 PM.
This article is licensed under a Creative Commons Attribution-NonCommercial 3.0 Unported Licence.

Lewis Basic Molten Salts: The Effects of Surface Chemistry, Reaction Conditions, and Molten Salt Composition, *J. Phys. Chem. C*, 2022, **126**, 1564–1580.

25 A. Gupta, J. C. Ondry, K. Lin, Y. Chen, M. H. Hudson, M. Chen, R. D. Schaller, A. J. Rossini, E. Rabani and D. V. Talapin, Composition-Defined Optical Properties and the Direct-to-Indirect Transition in Core–Shell In1−x Ga x P/ZnS Colloidal Quantum Dots, *J. Am. Chem. Soc.*, 2023, **145**, 16429–16448.

26 B. J. Beberwyck, Y. Surendranath and A. P. Alivisatos, Cation exchange: a versatile tool for nanomaterials synthesis, *J. Phys. Chem. C*, 2013, **117**, 19759–19770.

27 R. G. Pearson, Absolute electronegativity and hardness: application to inorganic chemistry, *Inorg. Chem.*, 1988, **27**, 734–740.

28 D. Lee, W. D. Kim, S. Lee, W. K. Bae, S. Lee and D. C. Lee, Direct Cd-to-Pb exchange of CdSe nanorods into PbSe/CdSe axial heterojunction nanorods, *Chem. Mater.*, 2015, **27**, 5295–5304.

29 L. De Trizio and L. Manna, Forging colloidal nanostructures via cation exchange reactions, *Chem. Rev.*, 2016, **116**, 10852–10887.

30 S. Koh, W. D. Kim, W. K. Bae, Y. K. Lee and D. C. Lee, Controlling ion-exchange balance and morphology in cation exchange from Cu3−x P nanoplatelets into InP crystals, *Chem. Mater.*, 2019, **31**, 1990–2001.

31 S. Koh, T. Eom, W. D. Kim, K. Lee, D. Lee, Y. K. Lee, H. Kim, W. K. Bae and D. C. Lee, Zinc–phosphorus complex working as an atomic valve for colloidal growth of monodisperse indium phosphide quantum dots, *Chem. Mater.*, 2017, **29**, 6346–6355.

32 Y.-B. Eun, G.-P. Jang, J.-H. Yang, S.-Y. Kim, Y.-B. Chae, M.-Y. Ha, D.-G. Moon and C.-K. Kim, Performance improvement of quantum dot light-emitting diodes using a ZnMgO electron transport layer with a core/shell structure, *Materials*, 2023, **16**, 600.

33 P. E. Blöchl, Projector augmented-wave method, *Phys. Rev. B: Condens. Matter Mater. Phys.*, 1994, **50**, 17953.

34 G. Kresse and J. Furthmüller, Efficient iterative schemes for ab initio total-energy calculations using a plane-wave basis set, *Phys. Rev. B: Condens. Matter Mater. Phys.*, 1996, **54**, 11169.

35 J. P. Perdew, K. Burke and M. Ernzerhof, Generalized gradient approximation made simple, *Phys. Rev. Lett.*, 1996, **77**, 3865.

36 S. Grimme, S. Ehrlich and L. Goerigk, Effect of the damping function in dispersion corrected density functional theory, *J. Comput. Chem.*, 2011, **32**, 1456–1465.

37 A. F. Wells, *Structural inorganic chemistry*, Oxford University Press, USA, 2012.

38 C. Brünig, S. Locmelis, E. Milke and M. Binnewies, Chemischer Transport fester Lösungen. 27. Mischphasenbildung und chemischer Transport im System ZnSe/GaAs, *Z. Anorg. Allg. Chem.*, 2006, **632**, 1067–1072.

39 S. Mishra, S. Daniele and L. G. Hubert-Pfalzgraf, Metal 2-ethylhexanoates and related compounds as useful precursors in materials science, *Chem. Soc. Rev.*, 2007, **36**, 1770–1787.

40 J. L. Bourque, M. C. Biesinger and K. M. Baines, Chemical state determination of molecular gallium compounds using XPS, *Dalton Trans.*, 2016, **45**, 7678–7696.

41 P. J. Larkin and A. Jackson, Interpretation of the Infrared Spectra of Metal-Stearate Salts, *Appl. Spectrosc. Pract.*, 2024, **2**(2), DOI: **10.1177/27551857241253834**.

42 C. Murray, D. J. Norris and M. G. Bawendi, Synthesis and characterization of nearly monodisperse CdE (E = sulfur, selenium, tellurium) semiconductor nanocrystallites, *J. Am. Chem. Soc.*, 1993, **115**, 8706–8715.

43 J. H. Yu, J. Joo, H. M. Park, S.-I. Baik, Y. W. Kim, S. C. Kim and T. Hyeon, Synthesis of quantum-sized cubic ZnS nanorods by the oriented attachment mechanism, *J. Am. Chem. Soc.*, 2005, **127**, 5662–5670.

44 J. Bang, J. Park, J. H. Lee, N. Won, J. Nam, J. Lim, B. Y. Chang, H. J. Lee, B. Chon, J. Shin, J. B. Park, J. H. Choi, K. Cho, S. M. Park, T. Joo and S. Kim, ZnTe/ZnSe (Core/Shell) Type-II Quantum Dots: Their Optical and Photovoltaic Properties, *Chem. Mater.*, 2010, **22**, 233–240.

45 Y. Kim, S. Ham, H. Jang, J. H. Min, H. Chung, J. Lee, D. Kim and E. Jang, Bright and uniform green light emitting InP/ZnSe/ZnS quantum dots for wide color gamut displays, *ACS Appl. Nano Mater.*, 2019, **2**, 1496–1504.

46 N. J. DeYonker and S. A. Shah, The role of core–valence electron correlation in gallium halides: a comparison of composite methods, *Theor. Chem. Acc.*, 2014, **133**, 1–11.

47 Y. Kim and S. Lee, Investigating the role of zinc precursor during the synthesis of the core of III–V QDs, *Chem. Commun.*, 2022, **58**, 875–878.

48 Y. Choi, C. Choi, J. Bae, J. Park and K. Shin, Synthesis of gallium phosphide quantum dots with high photoluminescence quantum yield and their application as color converters for LEDs, *J. Ind. Eng. Chem.*, 2023, **123**, 509–516.

49 P. Liu, Y. Lou, S. Ding, W. Zhang, Z. Wu, H. Yang, B. Xu, K. Wang and X. W. Sun, Green InP/ZnSeS/ZnS core multi–shelled quantum dots synthesized with aminophosphine for effective display applications, *Adv. Funct. Mater.*, 2021, **31**, 2008453.

50 D. Hahm, J. H. Chang, B. G. Jeong, P. Park, J. Kim, S. Lee, J. Choi, W. D. Kim, S. Rhee, J. Lim, D. C. Lee, C. Lee, K. Char and W. K. Bae, Design Principle for Bright, Robust, and Color-Pure InP/ZnSexS1−x/ZnS Heterostructures, *Chem. Mater.*, 2019, **31**, 3476–3484.

51 K. C. Dumbgen, J. Leemans, V. De Roo, M. Minjauw, C. Detavernier and Z. Hens, Surface Chemistry of InP Quantum Dots, Amine–Halide Co-Passivation, and Binding of Z-Type Ligands, *Chem. Mater.*, 2023, **35**, 1037–1046.

52 G. Almeida, R. F. Ubbink, M. Stam, I. du Fossé and A. J. Houtepen, InP colloidal quantum dots for visible and near-infrared photonics, *Nat. Rev. Mater.*, 2023, **8**, 742–758.

53 H.-L. Hu, H. Hao, X. Ren, Z.-Y. Chen, M. Liu, Y. Liu and F.-L. Jiang, Bright InP quantum dots by mid-synthetic modification with zinc halides, *Inorg. Chem.*, 2023, **62**, 2877–2886.

Open Access Article. Published on 18 March 2025. Downloaded on 3/10/2026 11:04:16 PM.
This article is licensed under a Creative Commons Attribution-NonCommercial 3.0 Unported Licence.

54 J. J. Calvin, J. K. Swabeck, A. B. Sedlak, Y. Kim, E. Jang and A. P. Alivisatos, Thermodynamic investigation of increased luminescence in indium phosphide quantum dots by treatment with metal halide salts, *J. Am. Chem. Soc.*, 2020, **142**, 18897–18906.

55 M. F. Prodanov, V. V. Vashchenko and A. K. Srivastava, Progress toward blue-emitting (460–475 nm) nanomaterials in display applications, *Nanophotonics*, 2021, **10**, 1801–1836.

56 J. Zhang, L. Wang, X. Zhang, G. Xie, G. Jia, J. Zhang and X. Yang, Blue light-emitting diodes based on halide perovskites: Recent advances and strategies, *Mater. Today*, 2021, **51**, 222–246.

57 C. Luo, C. Yan, W. Li, F. Chun, M. Xie, Z. Zhu, Y. Gao, B. Guo and W. Yang, Ultrafast thermodynamic control for stable and efficient mixed halide perovskite nanocrystals, *Adv. Funct. Mater.*, 2020, **30**, 2000026.

58 S. Ghosh, K. Das, K. Chakrabarti and S. De, Effect of oleic acid ligand on photophysical, photoconductive and magnetic properties of monodisperse SnO 2 quantum dots, *Dalton Trans.*, 2013, **42**, 3434–3446.

59 J.-Y. Yoo, S. A. Park, W. H. Jung, C. W. Lee, J. S. Kim, J.-G. Kim and B. D. Chin, Effect of dithiocarbamate chelate ligands on the optical properties of InP/ZnS quantum dots and their display devices, *Mater. Chem. Phys.*, 2020, **253**, 123415.

60 M. T. Frederick and E. A. Weiss, Relaxation of exciton confinement in CdSe quantum dots by modification with a conjugated dithiocarbamate ligand, *ACS Nano*, 2010, **4**, 3195–3200.

61 X. Yin, M. Shi, J. Wu, Y.-T. Pan, D. L. Gray, J. A. Bertke and H. Yang, Quantitative analysis of different formation modes of platinum nanocrystals controlled by ligand chemistry, *Nano Lett.*, 2017, **17**, 6146–6150.

62 Y.-J. Choi, C. W. Lee and J. S. Kim, Improvement of quantum dot light-emitting device efficiency by using multi-functional bipyridine ligands, *J. Korean Phys. Soc.*, 2020, **76**, 1121–1126.

63 M. Liu, Y.-Y. Wang, Y. Liu and F.-L. Jiang, Thermodynamic implications of the ligand exchange with alkylamines on the surface of CdSe quantum dots: The importance of ligand–ligand interactions, *J. Phys. Chem. C*, 2020, **124**, 4613–4625.

64 H. Yu, *Color Tuning for Perovskite Light-Emitting Diodes*, Linköping University Electronic Press, 2020.

65 S. Wang, Y. Guo, D. Feng, L. Chen, Y. Fang, H. Shen and Z. Du, Bandgap tunable Zn 1− x Mg x O thin films as electron transport layers for high performance quantum dot light-emitting diodes, *J. Mater. Chem. C*, 2017, **5**, 4724–4730.

66 S. A. Empedocles and M. G. Bawendi, Quantum-confined stark effect in single CdSe nanocrystallite quantum dots, *Science*, 1997, **278**, 2114–2117.

67 H. Lee, B. G. Jeong, W. K. Bae, D. C. Lee and J. Lim, Surface state-induced barrierless carrier injection in quantum dot electroluminescent devices, *Nat. Commun.*, 2021, **12**, 5669.

 This journal is © the Partner Organisations 2025